Journal of Non-Crystalline Solids 529 (2020) 119782

Contents lists available at ScienceDirect

Journal of Non-Crystalline Solids

journal homepage: www.elsevier.com/locate/jnoncrysol

Effects of crystallization on mechanical behavior and corrosion performance of a ductile $Zr_{68}Al_8Ni_8Cu_{16}$ bulk metallic glass

Nengbin Hua[a,b,c,1,*], Zhenlong Liao[a,c], Qianting Wang[a,c], Lei Zhang[a,c], Youxiong Ye[b], Jamieson Brechtl[d], Peter K Liaw[b]

[a] Department of Materials Science and Engineering, Fujian University of Technology, 350118 Fuzhou, China
[b] Department of Materials Science and Engineering, The University of Tennessee, 37996–2200 Knoxville, TN, United States
[c] Fujian Provincial Key Laboratory of Advanced Materials Processing and Application, 350118 Fuzhou, China
[d] The Bredesen Center for Interdisciplinary Research and Graduate Education, The University of Tennessee, 37996–3394 Knoxville, TN, United States

ARTICLE INFO

Keywords:
Bulk metallic glass
Annealing
Crystallization
Mechanical property
Corrosion behavior

ABSTRACT

The effects of heat treatment on the microstructures, crystallization kinetics, mechanical performance, and anti-corrosion behavior of a hypoeutectic $Zr_{68}Al_8Ni_8Cu_{16}$ bulk metallic glass (BMG) were studied. Through annealing, the precipitated phases were crystalline Zr_2Cu and Zr_2Ni. The total crystallinity was determined to be 10% and 77% for the samples annealed at 673 K and 713 K, respectively. The partial crystallization of the alloy leads to a dramatic deterioration in the ductility as compared to the as-cast BMG. Furthermore, the decrease in the ductility was accompanied by an increase in the crystallinity. The as-cast Zr-based BMG exhibited a greater corrosion resistance in the HCl solution than that of the annealed alloy. The depletion in the Zr and Al cation fractions of the surface oxidation film, which resulted from the precipitation of reactive nanocrystalline phases from the glassy matrix, is responsible for the reduced corrosion resistance.

1. Introduction

Because of their single-amorphous-phase structure, bulk metallic glasses (BMGs) generally exhibit a significantly higher strength than that of the crystalline alloys, which make them viable candidates as advanced structural materials [1-3]. However, the deformation of BMGs are localized into a single principal shear band [4-6]. Thus, BMGs are less-reliable owing to the limited room-temperature plasticity and catastrophic failure that occurs at relatively low applied strains. To overcome this drawback, a variety of attempts had been employed to improve the ductility of BMGs. For instance, introducing chemical or microstructural heterogeneity [7-14], developing BMGs with a high Poisson's ratio [15,16], and enhancing the free volume content of the glassy alloys [17,18].

Among various BMG systems, the Zr-based BMGs exhibit a combination of outstanding glass-forming ability (GFA), great mechanical performances, irradiation resistance, as well as anti-corrosion properties [19-22]. Recently, the hypo-eutectic Zr-based BMGs (with the Zr content above 65 at.%) were found to possess superior plasticity and ductility, as compared with those alloys that had either eutectic or near-eutectic compositions (usually has a content of about 50 at.% Zr) [15,16,23,24]. For instance, it has been reported that the $Zr_{70}Al_8Ni_{16}Cu_6$ BMG can withstand a relatively high compressive strain before fracture and also has a high fracture toughness [15]. Moreover, the hypo-eutectic BMG contains a structure which minimizes the degree of structural relaxation that may result in embrittlement. Furthermore, the hypo-eutectic BMG also shows a reduced stress corrosion cracking during the stress corrosion testing [25,26].

For engineering applications, the BMGs should have high chemical/electrochemical stability in industrial environments. As compared to the near-eutectic $Zr_{50}Al_{10}Cu_{40}$ BMG, the hypo-eutectic $Zr_{70}Al_8Ni_{16}Cu_6$ BMG shows better anti-corrosion performance in the chlorine-ion-containing solutions [26]. Based on the above result, in addition to their desirable mechanical properties, the hypo-eutectic BMGs are considered to possess great potential as advanced engineering materials [15,16,23-27].

Generally, however, the BMGs are thermodynamically metastable at room temperature [28]. When they are subjected to the thermal or mechanical activation, the crystallization of BMGs may occur, which substantially affect their chemical and mechanical performance. For example, it has been reported that the nanocrystalline/amorphous composites were fabricated in the Zr-based BMG systems via annealing-

* Corresponding authors at: Department of Materials Science and Engineering, Fujian University of Technology, 350118 Fuzhou, China
E-mail address: flower1982cn@126.com (N. Hua).
[1] Nengbin Hua, who will deal with the correspondence at all stages of paper reviews and publication.

https://doi.org/10.1016/j.jnoncrysol.2019.119782
Received 21 August 2019; Received in revised form 3 November 2019; Accepted 10 November 2019

induced-devitrification method. These composites demonstrated improved mechanical properties as compared to the fully amorphous materials [28-30]. On the contrary, some studies found that the precipitation of brittle crystalline phases during heat treatments led to the embrittlement of glassy alloys [31-33].

The corrosion resistance of BMGs can also be improved with the partial devitrification of the glassy structure [34,35]. With devitrification, the nanocrystalline-glass microstructure facilitates the generation of a protective surface film, which improves the overall corrosion resistance [34,35]. On the other hand, it has been reported that the annealing-induced-crystallization of the glassy matrix reduced the corrosion resistance of BMGs [36,37]. The presence of grain boundaries and dislocations that accompany crystallization, deteriorated the originally-homogeneous passive surface layer of the BMGs [36,37]. Therefore, it is quite important to study the influence of the crystallization behavior and kinetics of BMGs on their microstructure and properties.

To date, there are a variety of studies on the crystallization kinetics of Zr-based BMGs [38–40]. Nevertheless, there are virtually no studies concerning the effects of crystallization behaviors on the microstructure and properties of the hypoeutectic BMGs. In this context, the objectives of the present study are to (i) investigate the devitrification behavior of a hypoeutectic $Zr_{68}Al_8Ni_8Cu_{16}$ BMG, and (ii) gain a better understanding of the link between the annealing-induced microstructural evolution and the mechanical and chemical performance of the BMG. Furthermore, the results of the current work are anticipated to provide the foundational understanding and useful information relevant to mechanical and chemical properties of the hypoeutectic Zr-based BMG for future industrial applications.

2. Experiment methods

2.1. Materials characterization

The arc-melting method was employed to fabricate a $Zr_{68}Al_8Ni_8Cu_{16}$ (in atomic percent, or at.%) alloy. The pure metal (Zr: 99.8 wt.%, Cu: 99.98 wt.%, Ni: 99.95 wt.%, and Al: 99.999 wt.%) components were melted to prepare the master ingot in a Ti-gettered high-purity Ar atmosphere. Rod samples with a gage of ϕ 2 mm × 50 mm and plate specimens having a size of 1.5 mm × 12 mm × 40 mm were made by casting under the high purity Ar atmosphere. Melt spinning was carried out to prepare ribbon samples with a cross section of 0.02 × 1 mm^2. The structure of the as-cast and annealed (673 K and 713 K) (denoted as Zr68A, Zr68B, and Zr68C alloys, respectively) $Zr_{68}Al_8Ni_8Cu_{16}$ alloy specimens, was identified using X-ray diffraction (XRD) and transmission electron microscope (TEM) characterization techniques. For the XRD, the Bruker AXS D8 X-ray diffractometer (XRD) was used with a Cu K_α radiation together with the working voltage and current of 40 kV and 40 mA, respectively. As for the TEM characterization, a JEOL JEM-1200EX TEM was used. TEM samples were first mechanically ground to ~50 μm thick and then the twin-jet electropolishing method was performed to fabricate the TEM specimens. A chemical solution which contained 4% (in volume percent) $HClO_4$ ethanol was used for the electropolishing. The TEM specimens were cooled by liquid N_2 during the electropolishing.

2.2. Crystallization behavior and kinetics

The crystallization behavior was examined by annealing as-cast $Zr_{68}Al_8Ni_8Cu_{16}$ glassy ribbons in a NETZSCH DSC 404 C differential scanning calorimeter (DSC). A continuous flow of pure argon was introduced to prevent the oxidation of the samples at high temperatures over 673 K. For the annealing process, a heating rate of 20 K/min was used to raise the temperature from ambient to temperatures ranging from 673 K to 773 K). After heating to the maximum temperatures, the samples were immediately cooled. The microstructural evolution was examined using the XRD and TEM. The crystallinity were determined by dividing the area of crystal diffraction peaks by the total area of amorphous humb and crystal peaks using MDI Jade 7.0 software. The crystallization kinetics of the $Zr_{68}Al_8Ni_8Cu_{16}$ alloys was investigated by means of the continuous- and isothermal-heating techniques. The heating rates for the continuous heating ranged from 10 K/min to 40 K/min. For the isothermal DSC analysis, the samples were heated to the objective heating temperatures which ranged from 670 K to 676 K.

2.3. Mechanical property tests

Microhardness experiments were performed using a THVP-10 Vickers microhardness tester. Here, each sample was indented 5 times where the applied load was chosen as 300 gf, and the dwell time was 10 s. Room-temperature compressive and tensile properties were investigated using a DNS300 mechanical testing systems (MTS). For both tests, a strain rate of $2.1 \times 10^{-4}\ s^{-1}$ was used. The samples were machined by wire electrical discharge machining and then manually ground with using 2000 grit silicon carbide grinding paper. The sample geometries for the compression experiment were ϕ 2 mm × 4 mm. The working zone for the tension sample has a gage of 1.5 mm × 2 mm × 10 mm. The surface morphology of the deformed samples was characterized using a CS 3400 scanning electron microscope (SEM).

2.4. Corrosion behavior

To examine the corrosion behavior of the Zr68A, Zr68B, and Zr68C alloy samples, the immersion and electrochemical tests were performed. The samples used for the experiment had linear dimensions of 1.5 mm × 4 mm × 4 mm. The sample surface was polished using the 2000 grit silicon carbide grinding paper. For the experiment, samples were immersed in a 1 mol/L HCl solution for one week. After the immersion, the weight loss of the Zr68A, Zr68B, and Zr68C alloys was measured to calculate their corrosion rates. Furthermore, the surfaces of the immersed samples were examined by SEM and the compositions were verified by EDS. After an open circuit immersion in the 1 mol/L HCl solution, the potentiodynamic polarization measurements for the Zr68A, Zr68B, and Zr68C specimens were carried out using a three-electrode cell system. For the experiment, the working, counter, and reference electrodes corresponded to the alloy samples, platinum plate, and saturated calomel electrode (SCE), respectively. The surface morphologies and compositions of the polarized sample were characterized by SEM and EDS. To determine the mechanism of the polarization behavior, the composition of the oxide films for the Zr68A, Zr68B, and Zr68C specimens, after the 1 h immersion in the 1 mol/L HCl solution, were analyzed by an ESCALab250Xi X-ray photoelectron spectrometer (XPS).

3. Results and discussion

3.1. Structural characterization of the as-cast alloy sample

Fig. 1 displays the XRD pattern for the as-cast $Zr_{68}Al_8Ni_8Cu_{16}$ BMG (Zr68A) sample with a diameter of 2 mm. For this sample, no crystalline phase peaks can be observed in the pattern. The broad hump centered around ~37° indicates that the BMG is fully amorphous. The inset of Fig. 1 presents the continuous DSC curve of the Zr68A alloy under a heating rate of 20 K/min. The characteristic temperatures, including the glass transition temperature (T_g), onset crystallization temperature (T_x), and peak crystallization temperature (T_p), are marked by arrows in the DSC curve. As suggested by previous studies, the T_x and T_p correspond to the nucleation and growth of crystallization, respectively [29,30]. The endothermic and exothemic reactions in the DSC curve correspond to the glass transition and crystallization, respectively.

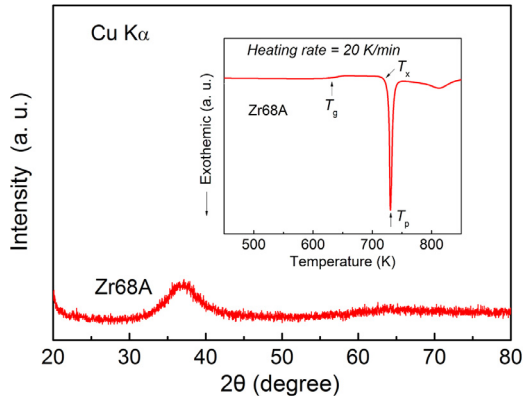

Fig. 1. XRD pattern for the as-cast Zr68A BMG. Inset is the continuous DSC curve of the Zr68A alloy.

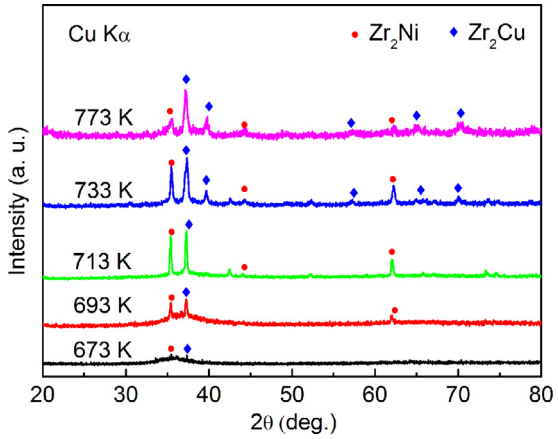

Fig. 2. XRD patterns for the Zr68A BMG after annealing to objective temperatures that ranged from 673 K to 773 K.

3.2. Crystallization behavior

Fig. 2 illustrates the XRD patterns for the Zr68A BMG after annealing to objective temperatures that ranged from 673 K to 773 K. After annealing the Zr68A alloy at 673 K, two crystalline phases were identified as the Zr_2Ni and Zr_2Cu precipitates with a crystallinity of 10%. Increasing the heating temperature up to 693 K results in an increase of the crystallinity of Zr_2Ni and Zr_2Cu phases to 20%. Furthermore, it was determined that the increase in the amount of these precipitates was not accompanied by the formation of new crystalline phases. Upon heating the Zr68A alloy at 773 K, the fraction of the Zr_2Cu phase further increases whereas that of the Zr_2Ni phase decreases.

Figs. 3(a)-(c) present the images of the transmission electron microscope (TEM) and selected area electron diffraction (SAED) of the (a) Zr68A (as-cast BMG), (b) Zr68B (annealed at 673 K), and (c) Zr68C (annealed at 713 K) alloys, respectively. The bright-field TEM image of the Zr68A show a homogeneous contrast, which suggests that the Zr68A BMG still contains a glassy structure. The broad halo in the SAED pattern (see the inset of Fig. 3(a)) further confirms the glassy structure of the Zr68A alloy. As shown in Fig. 3(b), the TEM image of the Zr68B alloy reveals that nanocrystals with sizes ranging from 5 to 100 nm are homogeneously dispersed in the glassy matrix. The inset SAED pattern along the [011] zone axis obtained for the crystallized alloy is indexed as the tetragonal Zr_2Cu phase. The analysis of the XRD data (see Fig. 2) indicates that as the heating temperature increases, the crystallinity of the crystal phase increases from 10% for sample Zr68B to 77% for sample Zr68C. However, the crystal size of the alloy remains on the order of nanometers for the Zr68C alloy, as identified by the TEM image in Fig. 3(c). The diffraction pattern in the inset of Fig. 3(c) corresponds to the [331] zone axis of the tetragonal Zr_2Cu phase.

3.3. Crystallization kinetics

Fig. 4(a) shows the continuous DSC plots of the Zr68A BMG for the heating rates of 10 - 40 K/min. The T_g, T_x, and T_p are marked by arrows in the DSC curves It can be observed that the values of the T_g, T_x, and T_p increase with an increasing heating rate. This result indicates that the glass transition and crystallization are dependent on the heating rate. There are several equations to determine the activation energies for the glass transition and crystallization of bulk metallic glasses, such as Kissinger equation, Ozawa equation, Augis-Bennett equation, and Lasocka equation, and so on [40]. It was found that there is no distinct difference in the values of the activation energies for the glass transition and crystallization of Zr-based bulk metallic glasses using different equations. Thus, the well-known Kissinger method was employed to study the crystallization kinetics of the Zr68A alloy. The Kissinger equation can be expressed as follows [24]:

$$\ln\left(\frac{T^2}{\phi}\right) = \frac{E}{RT} + C_1, \tag{1}$$

In Eq. (1), T is the above-mentioned characteristic temperature, like the T_g, T_x, and T_p, respectively. The ϕ, R, *and* C_1 correspond to the heating rate, the ideal gas constant, and an arbitrary constant, respectively. By solving for the Kissinger equation, the apparent activation energy, E_g, for the glass transition, E_x, and E_p for the onset and peak of crystallization for the Zr68A, were evaluated. These values were determined to be 264.7 KJ/mol, 245.6 KJ/mol, and 242.5 KJ/mol, respectively, and are displayed in Fig. 4(b). It can also be observed that the value of the E_p for the Zr68A is very similar to that of the E_x.

Moreover, the isothermal analysis was also carried out to further investigate the crystallization kinetics of the Zr68A alloy. Fig. 5(a) shows the DSC curves of the same BMG that was isothermally heated from 670 K to 674 K, which are the temperatures in the supercooled liquid interval. It can be seen that in all of the DSC curves, there is an incubation period before the onset of crystallization. Moreover, the incubation time increases with a decrease in the annealing temperature, indicating that the isothermal annealing process of the Zr68A BMG corresponds to a nucleation and growth transformation mechanism [29,30]. Fig. 5(b) shows a plot of the volume fraction, x, of the crystallites vs. the annealing time t for the crystallization process of the Zr68A BMG. The x and t data clearly shows a sigmoidal relationship, which has been reported on the isothermal crystallization kinetics for some other Zr-based BMGs, such as the $Zr_{60}Al_{10}Cu_{20}Ni_{10}$, $Zr_{62.5}Al_{12.1}Cu_{7.95}Ni_{17.45}$, and $Zr_{70}Al_{12.5}Fe_{17.5}$ amorphous alloys [17–21].

Recently, most research were focus on kinetics of crystallization in BMG using many methods such as Kissinger, Ozawa, and Augis-Bennett, and Johnson-Mehl-Avrami (JMA) equations. In fact, all these methods are based on the JMA theory which is usually used to describe the isothermal crystallization kinetics. In the present work, the JMA equation was introduced to analyze the nucleation, growth transformation behavior, and crystallization mechanism of the Zr68A BMG [31]. The JMA equation can be written as the following:

$$x(t) = 1 - \exp[-K(t-\tau)^n] \tag{2}$$

In Eq. (2), t and $x(t)$ are the annealing time and volume fraction, of the crystal phases, respectively. τ refers to the nucleation incubation time, which can be determined by deducting the time of the onset annealing temperature from that of the onset crystallization, n is the Avrami exponent, depending on the nature of the nucleation and growth of crystallization, and K is a reaction rate constant, which can be deduced from the Arrhenius equation:

$$K = K_0 \exp\left[-\frac{E_a}{RT}\right] \tag{3}$$

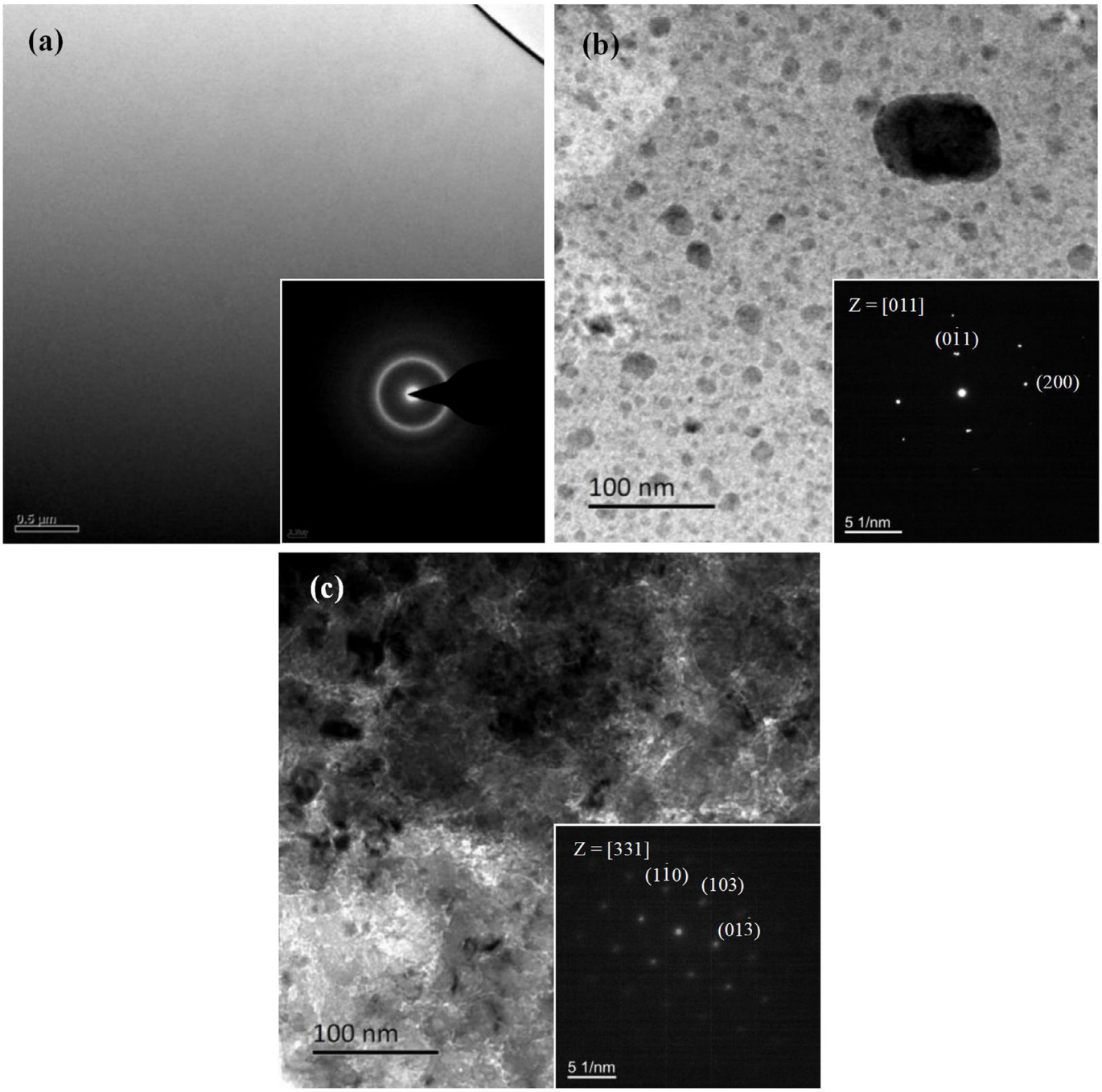

Fig. 3. TEM bright field images and SAED patterns for the (a) Zr68A (as-cast BMG), (b) Zr68B (annealed at 673 K), and (c) Zr68C (annealed at 713 K) alloys.

in which E_a is the activation energy for the crystallization process and K_0 is a constant. By integrating Eqs. (2) and (3) together, the JMA equation can be interpreted as:

$$\ln\left\{\ln\left[\frac{1}{1-x}\right]\right\} = n\ln K + n\ln(t-\tau) \tag{4}$$

According to Eq. (4), the Avrami exponent n is calculated as the slope of the plot for the $\ln\{\ln[1/(1-x)]\}$ as a function of the $\ln(t-\tau)$, as displayed in Fig. 5(c). The Avrami exponent n of the Zr68A BMG calculating from the JMA equation was found to be 2.17, 2.19, 2.09, and 2.10, for the Zr68A BMG samples that were annealed at temperatures of 670 K, 672 K, 674 K, and 676 K, respectively.

Generally, the Avrami exponent is a value that can characterize the nucleation and growth of crystalline phases in the metallic glasses during the isothermal annealing. An Avrami exponent of about 2.5 indicates that the crystallization exhibits a constant nucleation rate and the three-dimensional growth is controlled by diffusion [32]. However, if n is greater than 2.5, the diffusion-controlled three-dimensional growth mechanism will exhibit an increasing nucleation rate and vice versa [32]. In this work, the n value for the Zr68A BMG was found to vary from 2.09 to 2.19 at 670 - 676 K. Moreover, the average Avrami exponent is approximately 2.15, which implies that the crystallization process has a decreasing nucleation rate and the three-dimensional growth is controlled by diffusion.

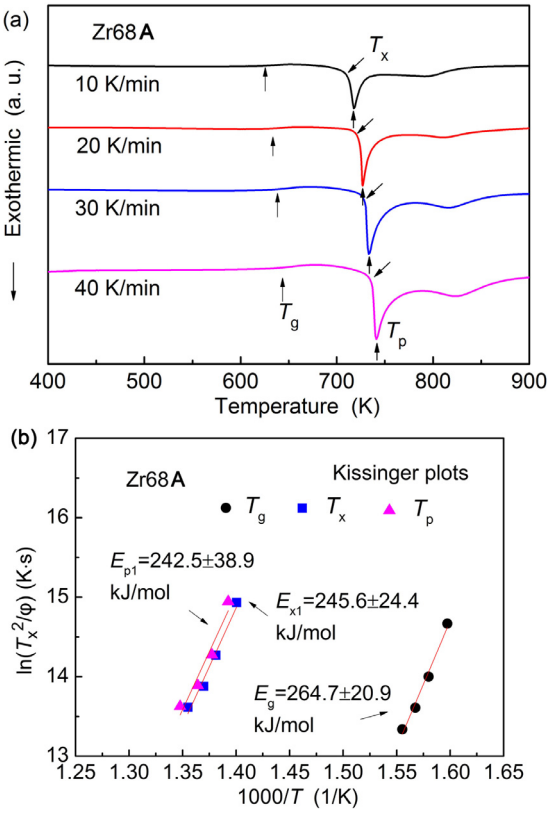

Fig. 4. (a) DSC curves of the Zr68A alloy under various heating rates of 10 - 40 K/min. (b) The apparent activation energies of the E_g, E_x, and E_p for the Zr68A BMG. .

3.4. Mechanical properties

The microhardness of the Zr68A, Zr68B, and Zr68C alloys is illustrated in Fig. 6, and are 455 HV (4.55 GPa), 430 HV (4.30 GPa), and 521 HV (5.21 GPa), respectively. The value of the microhardness for the Zr68 alloys shows a general increasing trend as the annealing temperature increases. Fig. 7(a) shows the compressive stress-strain curves for the Zr68A, Zr68B, and Zr68C alloys. The Zr68A BMG shows a relatively high yielding strength ($\sigma_{y,c}$) of 1480 MPa together with a large plastic strain ($\varepsilon_{p,c}$) of 9%. As for the Zr68B alloy (annealed at 673 K), it also exhibits a high yielding strength of 1500 MPa, but only exhibits a plastic strain of 3%. In contrast to these two alloys, the Zr68C alloy (heated at 713 K) fractures at a relatively-low strength of 750 MPa. Furthermore, no distinct yielding can be observed from the stress-strain curve of the same alloy, indicating a brittle fracture of the specimen during the compressive deformation.

Figs. 7(b)-(d) display the surface SEM images of the Zr68A, Zr68B, and Zr68C alloys after the compression. A variety of highly-branched shear bands (SBs) can be observed on the lateral surface of the Zr68A sample. This trend can prohibit the primary SBs propagating along localized shear direction [15-17], which enhances the ductility of the Zr68A alloy. The Zr68B alloy, which was annealed at 673 K, contains many branched and intercrossed SBs on the lateral surface. However, the density of the SBs in the Zr68B alloy is less than that of the Zr68A alloy. Moreover, the spacing between the primary and secondary SBs of the Zr68B alloy is larger than that of the Zr68A alloy. The greater spacing of the SBs in the Zr68B alloy corresponds to lesser degree of plasticity as compared to the Zr68A alloy, and is most likely a consequence of the heat treatment. On the contrary, the lateral surface of the Zr68C alloy, which was annealed at 713 K, shows very limited SBs after compression. Furthermore, the fracture morphology of the Zr68C alloy is characteristic of smooth river-like patterns that typically accompany brittle fracture.

Fig. 8(a) presents the stress-strain curves of the Zr68A, Zr68B, and Zr68C alloys that were subjected to tensile testing. The nearly zero plastic strain that was displayed by all of the Zr-based alloys before the fracture failure demonstrates a typical feature of the quasi-brittle behavior. However, the Zr68A BMG displays a large elastic strain of about 2.0% and a high tensile yield strength of 1580 MPa. It is thought that the annealing treatment reduces the yield strength of the Zr68A BMG. The Zr68B and Zr68C alloys display the yield strengths of 1500 MPa and 700 MPa, respectively.

Figs. 8(b)-(d) illustrate the lateral surface morphology of the fractured Zr68A, Zr68B, and Zr68C alloys after tensile deformation tests, respectively. The fracture morphology SEM characterization [in Fig. 8(b)] illustrates that a few SBs are present on the lateral surface of the Zr68A alloy after the tensile deformation. The secondary SBs that can be observed also formed during the tensile deformation process. Importantly, these SBs can hinders the propagation of the primary SBs along one localized shear direction. As a result, the primary and secondary shear bands are intercrossed, and distinct shear offsets on the tensile side are formed. This feature indicates that the Zr68A alloy exhibits a good crack growth resistance. By contrast, almost no SBs can be observed on the surface of the Zr68C alloy [see Fig. 8(d)], which is characteristic of brittle fracture.

3.5. Corrosion behaviors

Weight loss measurements were performed to determine the corrosion rate of the Zr68A, Zr68B, and Zr68C alloys that were immersed in the 1 mol/L HCl solution for one week. This weight loss was calculated using the equation: $R_{corr} = 8.76 \times 10^4 m/A\rho t$ (mm per year), where m is the weight loss (g), A is the total exposed surface area (mm^2) and ρ is the density of the sample (g/cm^3), and t is the immersion time (hour). The corrosion rates of the Zr68A, Zr68B, and Zr68C alloys were found to be 5.36 g/m^2h, 5.95 g/m^2h, and 7.95 g/m^2h, respectively (see Fig. 9). From the data it can be determined that the annealing treatment leads to an increase in the corrosion degradation of the Zr-based BMGs. After the immersion experiment was completed, the SEM was employed to examine the surfaces of the post-immersed Zr-based alloys.

Figs. 10(a)-(c) present the SEM images of the surface morphologies of the (a) Zr68A, (b) Zr68B, and (c) Zr68C alloys after the immersion corrosion testing. After immersion in the HCl solution for one week, the Zr68A alloy surface contains some corrosion pits that are several micrometers in size. As can be observed in Fig. 10(b), the corrosion pits on the surface of the Zr68B alloy have a honeycomb-like structure. As for the Zr68C alloy, the SEM imaging (see Fig. 10(c)) revealed that the surface had severely corroded during immersion in the HCl solution for one week. As indicated by the inset of Fig. 10(c), there are nano-scale pores which are dispersed inside the micron-scale corrosion pits. It is thought that these pores are related to the preferential dissolution of the Zr68C alloy [26,27]. The EDS was then performed to compare the chemical composition of the corrosion pit with the surrounding surface. These regions were labelled A and B (alloy Zr68A), C and D (alloy Zr68B), and E and F (Zr68C) in the inset of Figs. 10(a)-(c), respectively. It is noted that the A, C, and E refer to the regions in the corrosion pits whereas the B, D, and F locate in the regions outside the corrosion pits. The results of the EDS analysis for the aforementioned regions are shown in Fig. 11. The corrosion pits of the Zr-based alloys were found to consist primarily of Zr, Al, Ni, Cu, and O. It is seen that these regions (labelled as A, C, and E) are O-enriched as compared to surrounding surface. From these results it is suggested that the high fraction of O is attributed to the oxide corrosion product that is located outside of the corrosion pits.

Fig. 12 shows the potentiodynamic polarization curves for the Zr68A, Zr68B, and Zr68C alloys that were immersed in the 1 mol/L HCl solution. From the Fig. 12 it can be seen that the Zr68A alloy has the most positive corrosion potential ($E_{corr} = -0.25$ V). The sampled that

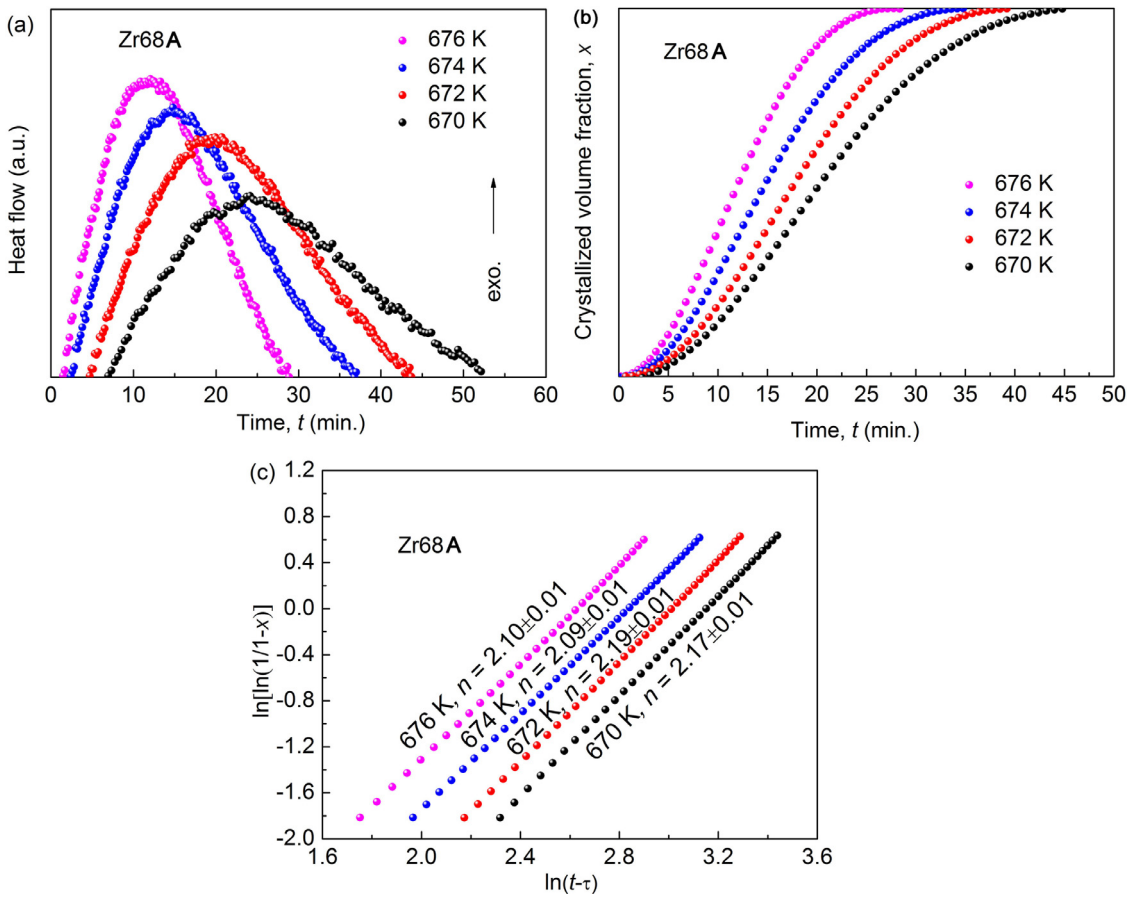

Fig. 5. (a) DSC curves of the Zr68A BMG isothermally heated at temperatures of 670 K, 672 K, 674 K, and 676 K. (b) Volume fraction of the crystals x of the Zr68A BMG as a function of the annealing time t. (c) Avrami exponent n deduced by the JMA equation.

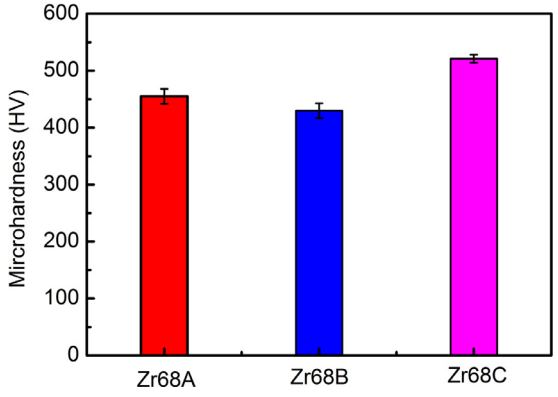

Fig. 6. The microhardness of the Zr68A, Zr68B, and Zr68C alloys.

was annealed at 673 K (Zr68B alloy) displayed a positive corrosion potential of −0.254 V during the experiment, which was similar to the value for the Zr68A alloy. The sample that was annealed at 713 K (alloy Zr68C) exhibited a potential value of −0.274 V, signifying a notable shift towards more cathodic values. It can be surmised from the polarization curves that the Zr-based alloys actively dissolutes as long as the potential reaches the corrosion potential, owing to the unstable oxide films that form on the surface of the Zr-based alloys while immersed in the chloride-ions-containing solutions. After the potential exceeded E_{corr} the current density increased rapidly. Furthermore, annealing leads to an increase of the corrosion current density (i_{corr}) from 1.42×10^{-3} A/m^2 for the as-cast Zr68A sample to 2.55×10^{-3} A/m^2 and 1.68×10^{-2} A/cm^2 for Zr68B and Zr68C alloys, respectively. This result demonstrates that the corrosion resistance of the Zr68A BMG is reduced because of the microstructural change induced by annealing.

In this study, the XPS analysis was performed on the Zr-based alloy specimens immersed in the HCl solution at 298 K for 1 h to investigate the chemical compositions of the passive films. Figs. 13(a)-(f) present the XPS spectra for both the survey [Fig. 13(a)] and narrow scans [Fig. 13(b)-(f)]. As can be seen, the results show that the O, Zr, Al, Cu, and Ni are on the surfaces of the Zr68A, Zr68B, and Zr68C. The C 1 s peaks are from the carbon contamination of the specimen. The O 1 s peaks correspond to O^{2-} and OH. The peaks for the Zr3d, Al2p, Ni2p, and Cu2p states represent both the oxidized and metallic states. The oxidized states are associated with the surface films whereas the metallic states correspond to the alloy substrate. The elemental distributions of the surface film for the Zr-based alloys, as measured by XPS, are shown in Fig. 14. The results show that the surface oxide film is primarily enriched with O, Zr, and Al. After annealing at 673 K, the cation fractions of the Zr and Al in the Zr68B alloy are approximately equal to that of the Zr68A. The cation fractions of Zr and Al for the sample annealed at 713 K (Zr68C) are smaller as compared to the other two samples. The reduction in the corrosion resistance of the Zr-based alloys as a resulting of the annealing can be ascribed to the decreasing cation fractions of the protective Zr and Al contained in the surface film oxides.

4. Discussion

4.1. Effects of crystallization on the mechanical properties of the hypoeutectic zr-based bmg

The BMGs usually show a limited plastic strain before fracture at

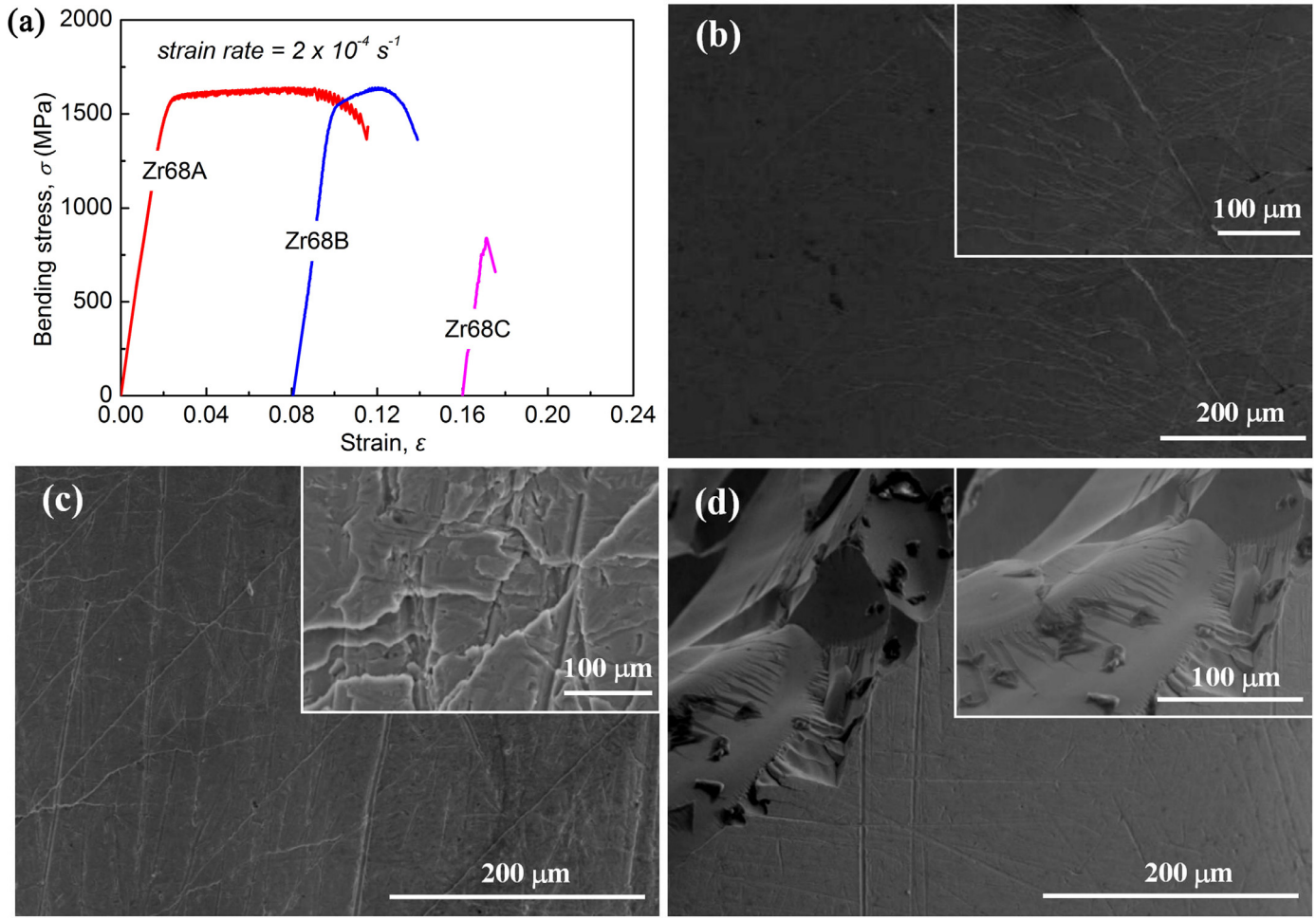

Fig. 7. (a) Stress-strain curves of the Zr68A, Zr68B, and Zr68C alloys tested under compression. SEM images of the surface morphology for the (b) Zr68A, (c) Zr68B, and (d) Zr68C alloys subjected to the compressive deformation.

room temperature, owing to the localized deformation in shear bands [4-6]. There are a variety of studies on the effects of crystalline phases on the plasticity of BMGs. It has been reported that the in-situ formation of ductile crystalline phases during the casting process can enhance the plasticity of metallic glasses. A composite structure can therefore be an effective way to improve the ductility of BMGs [10,11]. It has been reported that Zr-based metallic glass composites, which contain ductile bcc or B2 phases, exhibit relatively large plasticity during both compression and tensile tests [10,11]. However, in most cases, annealing-induced precipitation of crystalline phases usually lead to the decrease of mechanical properties, namely the annealing-induced-brittleness. The plasticity of metallic glasses is dependent on the volume fraction and the microstructures of crystalline phases [41-44]. Also, the effect of devitrification of the BMGs on their mechanical behavior through controlled annealing treatment were also studied. For instance, it was reported that crystalline $Zr_{55}Cu_{30}Al_{10}Ni_5$ alloy exhibits the higher Young's modulus and hardness than those of the as-cast metallic glass [41].

It has been reported that isothermal annealing was introduced as an attempt to enhance the mechanical properties of a $Zr_{65}Cu_{17.5}Fe_{10}Al_{7.5}$ BMG. After annealing at 573 K for 1.0 h, the alloy displays a large plastic strain of 7.1% as well as a high strength, owing to the precipitation of the 5–12 nm nanocrystallites in the glassy matrix [42]. Similar results were obtained for other BMGs after crystallization [43,44]. Qin et al. [44] found that in a $Ti_{40}Zr_{10}Cu_{36}Pd_{14}$ BMG which contained thermally induced nanocrystalline/metallic glass composites, it exhibited a yield strength and plastic strain of 2100 MPa and 0.8%, respectively. However, with the increase of the annealing temperature, the compressive strength of the composites decreased in proportion with the increasing degree of crystallization.

The ductility of metallic glasses is closely related to the free volumes in their structure. Upon annealing at high temperature, the fraction of free volumes is decreased and the ductility of metallic glass is reduced [25]. Moreover, it was found that the hypoeutectic Zr-based BMG has relatively great resistance to relaxation-induced embrittlement. It has been reported that the hypoeutectic $Zr_{60}Cu_{30}Al_{10}$ BMG has relatively good mechanical properties, such as high tensile fracture strength and great resistance to relaxation-induced embrittlement [25]. In this study, the high-Zr-bearing $Zr_{68}Al_8Ni_8Cu_{16}$ BMG, which exhibits a good combination of high yield strength and plastic strain (1.48 GPa and 9%, respectively), are potentially viable candidates for engineering applications. It is well known that the mechanical performance of BMGs and their composites are strongly dependent on their microstructures. Therefore, the relationship between the crystallization and mechanical properties of the hypoeutectic BMGs requires intensive investigation to further understand their suitability for engineering applications.

It is concluded that the Zr_2Cu and Zr_2Ni phases precipitate out from the amorphous matrix of the BMG through annealing. The crystallinity are determined to be 0, 10%, and 77% for the Zr68A, Zr68B, and Zr68C alloys, respectively. Based on the compressive and tensile deformation results, the fully amorphous Zr68A alloy displays the excellent mechanical properties, including the largest plastic strain of 9% and high yield strength of 1480 MPa. After annealing at 673 K, the Zr68B alloy exhibits a reduced plastic strain of 3% without losing its strength. After

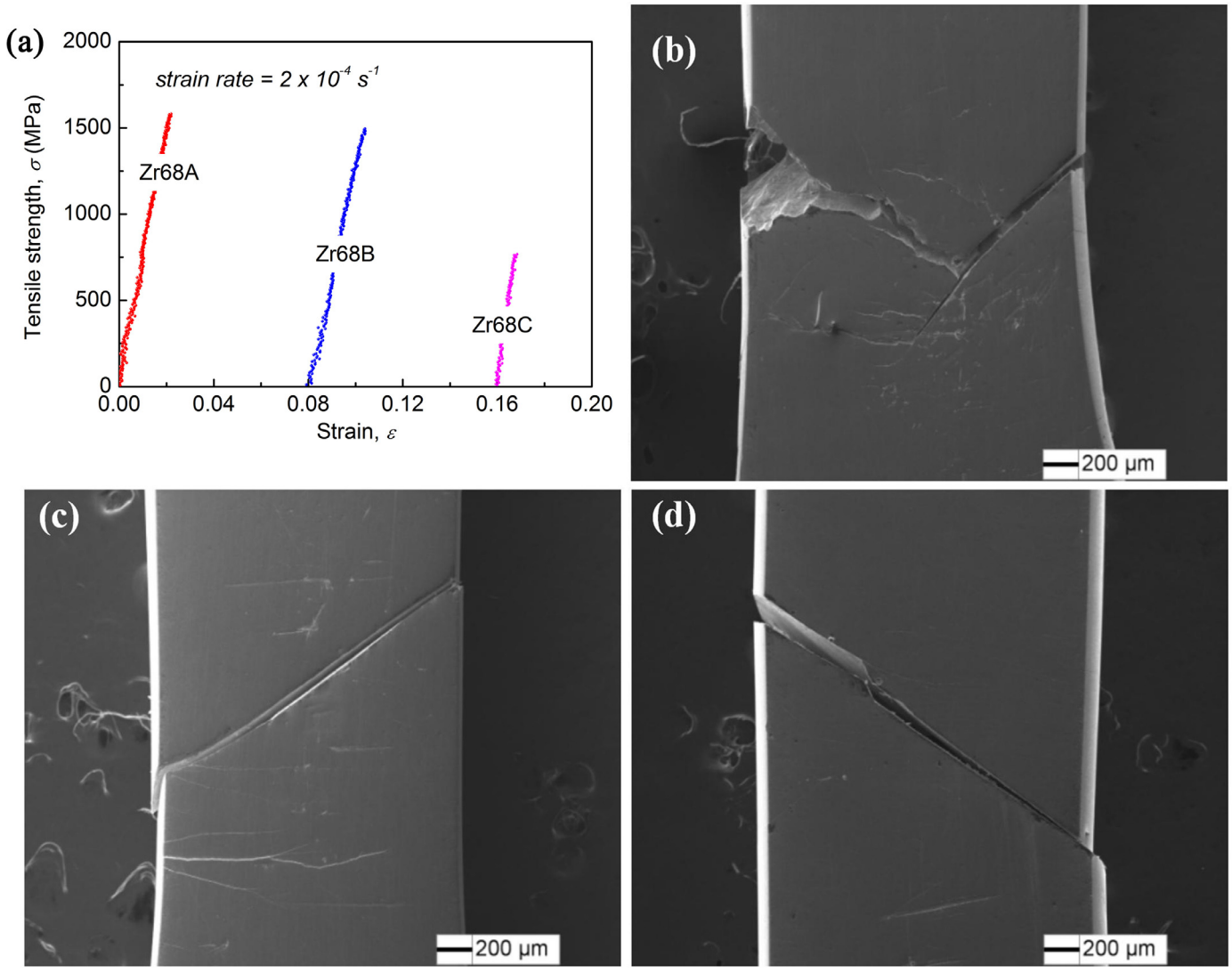

Fig. 8. (a) Stress-strain curves of the Zr68A, Zr68B, and Zr68C alloys under tensile test. Surface morphology SEM images of the (b) Zr68A, (c) Zr68B, and (d) Zr68C alloys after the tensile deformation.

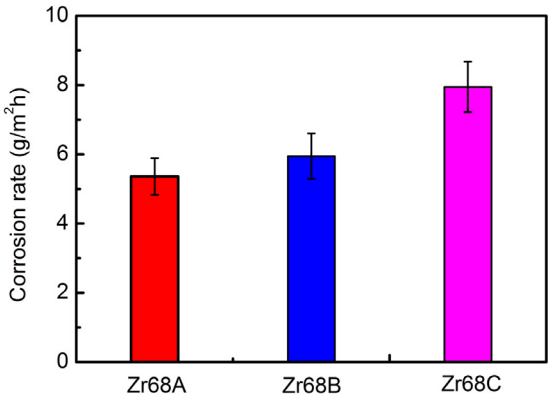

Fig. 9. Corrosion rates of the Zr68A, Zr68B, and Zr68C alloys in the 1 mol/L HCl solution. .

annealing at 713 K, the crystallization leads to a progressive decrease in the strength of the alloy (750 MPa) and a nearly zero plastic strain. This decrease in the strength and plasticity is a typical characteristic of the annealing-induced-embrittlement. As seen in Figs. 2 and 3, increasing the annealing temperature did not change the amount of precipitating Zr_2Cu and Zr_2Ni crystalline phases in the glass. However, the crystallinity increase from 10% to 77% as the annealing temperature increases from 673 K to 713 K. Thus, it can be concluded that the fractions of the precipitated crystalline phases significantly affect the mechanical properties of the hypoeutectic Zr-based BMGs. This decrease in the strength and plasticity is a typical characteristic of the annealing-induced-embrittlement. For one thing, the free volume is annihilated during the annealing process. For another thing, the precipitated brittle intermetallic phases further deteriorate the strength and plasticity of the Zr-based BMGs.

4.2. Effects of crystallization on the corrosion resistance of the hypoeutectic zr-based bmg

Apart from the alloying elements, the microstructure also takes a principal role in determining the corrosion resistance of metallic alloys [34-37]. Generally, the BMGs exhibit the higher corrosion resistance than that of conventional crystalline alloys. This enhanced corrosion resistance of the BMGs arises from its amorphous structure, which lacks dislocations and grain boundaries that are susceptible to corrosion attacks [1,2,26].

Recently, the corrosion resistance of these thermally crystallized BMGs have been studied. It has been reported that partially

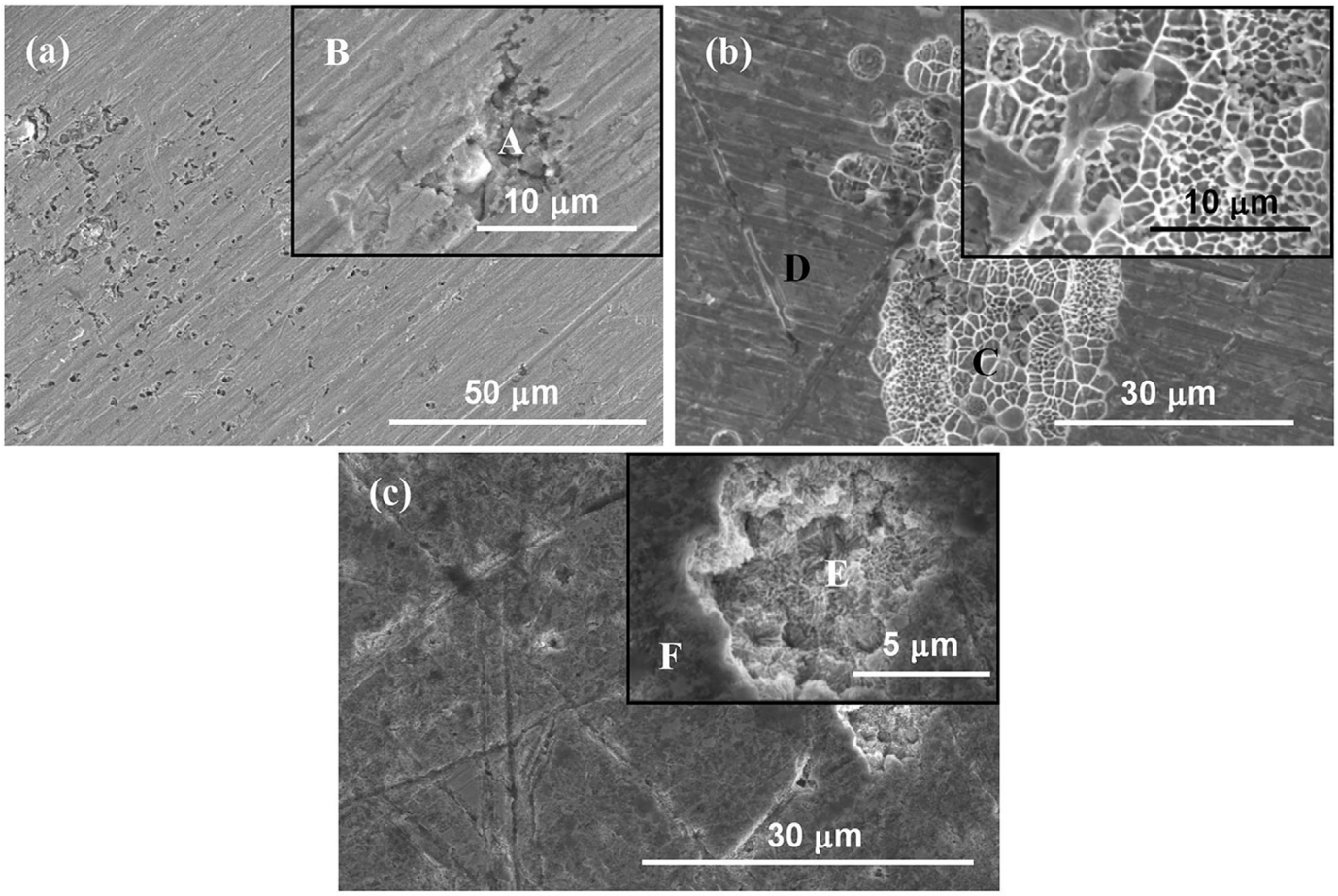

Fig. 10. Surface SEM morphology after the immersion test for the (a) Zr68A, (b) Zr68B, and (c) Zr68C alloys, respectively.

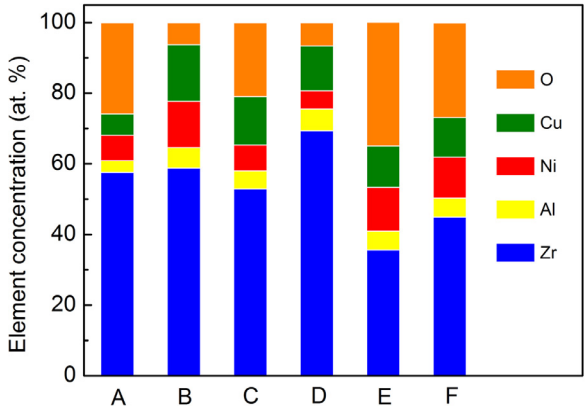

Fig. 11. EDS composition results on typical regions of the corrosion pits.

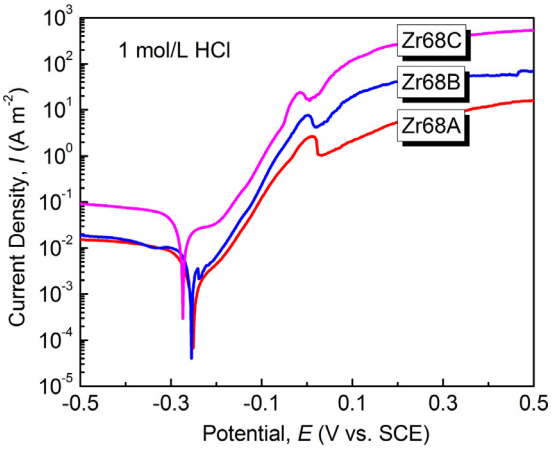

Fig. 12. Potentiodynamic polarization curves of the Zr68A, Zr68B, and Zr68C alloys in the 1 mol/L HCl solution.

crystallizing a BMG can either improve or reduce its corrosion resistance [34-37]. For instance, the corrosion response of the $Zr_{47.5}Cu_{47.5}Al_5$ BMG and its composites in the seawater solution have been investigated. The results show that the as-cast BMG composite has a microstructure consisting of CuZr nanocrystals that are surrounded glassy matrix. Moreover, the as-cast BMG composite possesses a greater anti-corrosion capacity than that of the BMG and the as-annealed composite [45]. Meanwhile, the pitting corrosion resistance of a $Zr_{65}Cu_{17.5}Fe_{10}Al_{7.5}$ BMG has been enhanced by annealing, which is attributed to the formation of nanocrystallites with diameters of 5 - 12 nm in the glassy matrix [42]. Similarly, Li et al. [46] reported that the heat treatment results in the precipitation of the nanocrystalline phases in the $Fe_{73.5}Si_{13.5}B_9Nb_3Cu_1$ amorphous alloy. The composite structure improved its corrosion resistance in a 3.5 wt.% NaCl solution because it formed a protective passive film. However, Wu et al. [47] found that nanocrystalline $Fe_{40}Si_{38}B_{18}Mo_4$ led to a reduced corrosion resistance in the Fe based metallic glass when immersed in a 3.5 wt.% NaCl solution during the galvanic cell reaction. Therefore, the effects of annealing on the corrosion behaviors of the BMGs requires further investigation.

It has been reported that the Zr-based BMGs are usually subject to the pitting corrosion in the chloride-ion-containing solutions

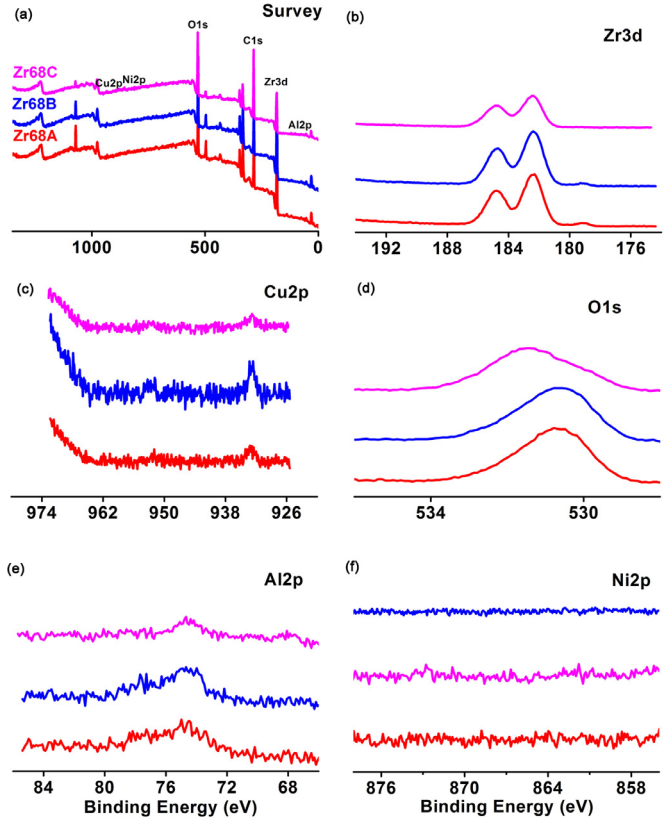

Fig. 13. The XPS spectra of the Zr68A, Zr68B, and Zr68C alloys for both the survey (a) and narrow scans (b)-(f).

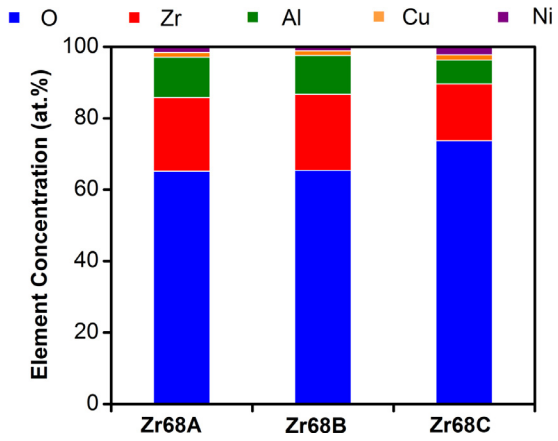

Fig. 14. The chemical compositions of the surface film for the Zr-based alloys measured by XPS.

[26,27,42,48]. Furthermore, the $Zr_{41.2}Ti_{13.8}Cu_{12.5}Ni_{10}Be_{22.5}$ BMG was exhibited low resistance to stress corrosion cracking in the neutral 0.5 M NaCl solution [49]. The $Zr_{55}Cu_{30}Al_{10}Ni_5$ BMG also showed high fatigue crack growth rates in the NaCl solution [50]. Nevertheless, it was recently found that the hypoeutectic $Zr_{70}Cu_6Al_8Ni_{16}$ BMG showed high resistance to stress corrosion cracking under the same condition [51]. The XPS analysis revealed that the exceptional anti-corrosion property of the $Zr_{70}Cu_6Al_8Ni_{16}$ BMG resulted from the homogeneous and protective Zr-enriched passive film [51].

Nonetheless, the effects of crystallization on the corrosion resistance of the hypoeutectic Zr-based BMGs are still not fully understood. From the immersion and electrochemical testing results, it is observed that the as-cast Zr68A glassy alloy displays the excellent anti-corrosion performance. With an increase in the annealing temperature the volume fraction of the crystal increases, resulting in a progressively reduced corrosion resistance. It is suggested that the structure and composition of the precipitated crystalline Zr_2Cu and Zr_2Ni phases are responsible for the low corrosion resistance in the highly-crystallized alloy. It has been reported that [26,27] galvanic corrosion may occur between the Zr_2Cu and Zr_2Ni nanocrystalline phases and the glassy matrix.

The good anti-corrosion properties of the Zr68A BMG can be ascribed to the chemistry and microstructure of the alloy surface. For instance, the Zr-based BMG contains a homogeneous glassy structure without crystalline defects, which results in the formation of a stable passive film. The stable passive film can protect the BMG from an aggressive environment and, hence, contribute to the excellent corrosion resistance of the alloy. As illustrated in Fig. 14, with the increasing annealing temperature up to 713 K, the fraction of Zr and Al contained in the surface film of the Zr-based alloys significantly reduces. Since the ZrO_2 and Al_2O_3 oxides films are dense and stable, they can reduce the attack of the chloride-containing solution. Thus, the greatly reduced corrosion resistance of the Zr68C alloy, as compared to that of the Zr68A and Zr68B alloys, results from the depletion of the Zr- and Al-oxide surface film.

5. Conclusions

The present study investigated the evolution of the microstructure, crystallization kinetics, mechanical performance, and corrosion characteristics of a $Zr_{68}Al_8Ni_8Cu_{16}$ BMG that was annealed at temperatures of 673 and 713 K.

(1) The crystal Zr_2Cu and Zr_2Ni phases were observed in the $Zr_{68}Al_8Ni_8Cu_{16}$ BMG after heating. The total crystallinity of these crystalline phases were determined to be 10% and 77% for the Zr68B (annealed at 673 K) and Zr68C (annealed at 713 K) alloys, respectively.
(2) Under isothermal annealing, the average Avrami exponent of the Zr68A alloy modeled by the JMA equation is about 2.1, indicating that the crystallization is mainly governed by a diffusion-controlled three-dimensional growth with a decreasing nucleation rate.
(3) The Zr68A alloy exhibits the high compressive yield strength of 1.48 GPa and tensile yield strength of 1.5 GPa. Partial crystallization led to progressively deteriorated mechanical properties. The fracture strength and plastic strain of the Zr68C alloy are 0.75 GPa and 0%, respectively. The annealing-induced-embrittlement can be ascribed to the precipitation of Zr_2Cu and Zr_2Ni intermetallics from the glassy matrix.
(4) The immersion and potentiodynamic polarization testing results show that the Zr68A alloy exhibits the highest corrosion resistance in the HCl solution. With an increase in the annealing temperature, the corrosion resistance becomes progressively reduced. The results suggested that the increasing degree of partial crystallization of reactive intermetallic phases in the glass matrix could be responsible for the reduced corrosion resistance.

Declaration of Competing Interest

The authors declare that they have no known competing financial interests or personal relationships that could have appeared to influence the work reported in this paper.

Acknowledgement

The present work was supported by the National Natural Science Foundation of China (51401053 and 21701024), the Natural Science Foundation of Fujian Province (2018J01629), the New Century Excellent Talents in University of Fujian Province (GY-Z17066), and the Scientific Research Project of Fujian University of Technology (GY-

Z17152). N.B. Hua acknowledged the China Scholarship Council (CSC) for sponsoring his visit to the University of Tennessee (UT) where the present work was partly conducted. Y.X. Ye would like to acknowledge funding from the State of Tennessee and Tennessee Higher Education Commission (THEC) through their support of the Center of Materials Processing (CMP). PKL thanks the support from the National Science Foundation (DMR-1611180 and 1809640) with the program directors, Drs. G. Shiflet and D. Farkas.

References

[1] W.H. Wang, C. Dong, C.H. Shek, Bulk metallic glasses, Mater. Sci. Eng. R 44 (2004) 45–89 https://doi.org/10.1016/j.mser.2004.03.001.
[2] A. Inoue, A. Takeuchi, Recent development and application products of bulk glassy alloys, Acta Mater. 59 (2011) 2243–2267 https://doi.org/10.1016/j.actamat.2010.11.027.
[3] C.A. Schuh, T.C. Hufnagel, U. Ramamurty, Mechanical behavior of amorphous alloys, Acta Mater. 55 (2007) 4067–4109 https://doi.org/10.1016/j.actamat.2007.01.052.
[4] T.C. Hufnagel, C.A. Schuh, M.L. Falk, Deformation of metallic glasses: recent developments in theory, simulations, and experiments, Acta Mater. 109 (2016) 375–393 https://doi.org/10.1016/j.actamat.2016.01.049.
[5] J. Schroers, W.L. Johnson, Ductile bulk metallic glass, Phys. Rev. Lett. 93 (2004) 255506https://doi.org/10.1103/physrevlett.93.255506.
[6] Z.Q. Liu, Z.F. Zhang, Strengthening and toughening metallic glasses: the elastic perspectives and opportunities, J. Appl. Phys. 115 (2014) 163505https://doi.org/10.1063/1.4872249.
[7] J. Das, M.B. Tang, K.B. Kim, R. Theissmann, F. Baier, W.H. Wang, J. Eckert, "Work-hardenable" ductile bulk metallic glass, Phys. Rev. Lett. 94 (2005) 205501https://doi.org/10.1103/PhysRevLett.94.205501.
[8] Y.H. Liu, R.J.Wang G.Wang, D.Q. Zhao, M.X. Pan, W.H. Wang, Super plastic bulk metallic glasses at room temperature, Science 315 (2007) 1385–1388 https://doi.org/10.1126/science.1136726.
[9] K.B. Kim, J. Das, F. Baier, Heterogeneity of a $Cu_{47.5}Zr_{47.5}Al_5$ bulk metallic glass, Appl. Phys. Lett. 88 (2006) 051911https://doi.org/10.1063/1.2171472.
[10] Y. Wu, Y.H. Xiao, G.L. Chen, C.T. Liu, Z.P. Lu, Bulk metallic glass composites with transformation-mediated work-hardening and ductility, Adv. Mater. 22 (2010) 2770–2773 https://doi.org/10.1002/adma.201000482.
[11] D.C. Hofmann, J.Y. Suh, A. Wiest, G. Duan, M.L. Lind, M.D. Demetriou, W.L. Johnson, Designing metallic glass matrix composites with high toughness and tensile ductility, Nature 451 (2008) 1085–1089 https://doi.org/10.1038/nature06598.
[12] T. Wang, Y. Wu, J.J. Si, Y.H. Liu, X.D. Hui, Plasticizing and work hardening in phase separated Cu-Zr-Al-Nb bulk metallic glasses by deformation induced nanocrystallization, Mater. Des. 142 (2018) 74–82 https://doi.org/10.1016/j.matdes.2018.01.003.
[13] D.H. Kim, W.T. Kim, E.S. Park, N. Mattern, J. Eckert, Phase separation in metallic glasses, Prog. Mater. Sci 58 (2013) 1103–1172 https://doi.org/10.1016/j.pmatsci.2013.04.002.
[14] Y.L. Ren, R.L. Zhu, J. Sun, J.H. You, K.Q. Qiu, Phase separation and plastic deformation in an Mg-based bulk metallic glass, J. Alloy. Compd. 493 (2010) L42–L46 https://doi.org/10.1016/j.jallcom.2009.12.195.
[15] Y. Yokoyama, K. Fujita, A.R. Yavari, A. Inoue, Malleable hypoeutectic Zr-Ni-Cu-Al bulk glassy alloys with tensile plastic elongation at room temperature, Philos. Mag. Lett 89 (2009) 322–334 https://doi.org/10.1080/09500830902873575.
[16] X. Hui, S.N. Liu, S.J. Pang, L.C. Zhuo, T. Zhang, G.L. Chen, Z.K. Liu, High-zirconium-based bulk metallic glasses with large plasticity, Scripta Mater. 63 (2010) 239–242 https://doi.org/10.1016/j.scriptamat.2010.03.065.
[17] L.Y. Chen, Z.D. Fu, G.Q. Zhang, X.P. Hao, Q.K. Jiang, X.D. Wang, Q.P. Cao, H. Franz, Y.G. Liu, H.S. Xie, S.L. Zhang, B.Y. Wang, Y.W. Zeng, J.Z. Jiang, New class of plastic bulk metallic glass, Phys. Rev. Lett 100 (2008) 175501https://doi.org/10.1103/PhysRevLett.100.075501.
[18] W. Zhou, J.Q. Hu, W.P. Weng, L.Y. Gao, G.Y. Xu, Enhancement of plasticity in Zr-Cu-Ni-Al-Ti bulk metallic glass by heterogeneous microstructure, J. Non-Cryst. Solids 481 (2018) 530–536 https://doi.org/10.1016/j.jnoncrysol.2017.11.042.
[19] N.B. Hua, T. Zhang, Glass-forming ability, crystallization kinetics, mechanical property, and corrosion behavior of Zr-Al-Ni-Ag glassy alloys, J. Alloy. Compd. 602 (2014) 339–345 https://doi.org/10.1016/j.jallcom.2014.03.015.
[20] A.G. Perez-Bergquist, H. Bei, K.J. Leonard, Y. Zhang, S.J. Zinkle, Effects of ion irradiation on $Zr_{52.5}Cu_{17.9}Ni_{14.6}Al_{10}Ti_5$ (BAM-11) bulk metallic glass, Intermetallics 53 (2014) 62–66 https://doi.org/10.1016/j.intermet.2014.04.016.
[21] J. Brechtl, S. Agarwal, M.L. Crespillo, T. Yang, H. Bei, S.J. Zinkle, Evolution of the microstructural and mechanical properties of BAM-11 bulk metallic glass during ion irradiation and annealing, J. Nucl. Mater (2019), https://doi.org/10.1016/j.jnucmat.2019.06.010.
[22] N.B. Hua, S.J. Pang, Y. Li, J.F. Wang, R. Li, K. Georgarakis, A.R. Yavari, G. Vaughan, T. Zhang, Ni- and Cu-free Zr-Al-Co-Ag bulk metallic glasses with superior glass forming ability, J. Mater. Res. 26 (2011) 539–546 https://doi.org/10.1557/jmr.2010.65.
[23] Y.H. Li, W. Zhang, C. Dong, J.B. Qiang, K. Yubuta, A. Makino, A. Inoue, Unusual compressive plasticity of a centimeter-diameter Zr-based bulk metallic glass with high Zr content, J. Alloy. Compd. 504S (2010) S1–S5 https://doi.org/10.1016/j.jallcom.2010.02.069.
[24] N.B. Hua, R. Li, J.F. Wang, T. Zhang, Biocompatible Zr-Al-Fe bulk metallic glasses with large plasticity, Sci. China Phys. Mech. Astron 55 (2012) 1664–1669 https://doi.org/10.1007/s11433-012-4831-5.
[25] Y. Yokoyama, T. Yamasaki, P.K. Liaw, A. Inoue, Study of the structural relaxation-induced embrittlement of hypoeutectic Zr-Cu-Al ternary bulk glassy alloys, Acta Mater. 56 (2008) 6097–6108 https://doi.org/10.1016/j.actamat.2008.08.026.
[26] A. Kawashima, K. Ohmura, Y. Yokoyama, A. Inoue, The corrosion behaviour of Zr-based bulk metallic glasses in 0.5M NaCl solution, Corros. Sci. 53 (2011) 2778–2784 https://doi.org/10.1016/j.corsci.2011.05.014.
[27] N.B. Hua, L. Huang, W.Z. Chen, W. He, T. Zhang, Biocompatible Ni-free Zr-based bulk metallic glasses with high-Zr-content: compositional optimization for potential biomedical applications, Mater. Sci. Eng. C 44 (2014) 400–410 https://doi.org/10.1016/j.msec.2014.08.049.
[28] J. Saida, M. Matsushita, A. Inoue, Nano icosahedral quasicrystals in Zr-based glassy alloys, Intermetallics 10 (2002) 1089–1098 https://doi.org/10.1016/S0966-9795(02)00142-5.
[29] V. Venkatesh, G.K. Mondal, Effect of cast temperature, size and annealing condition on the serrated flow during nano-indentation of Zr-based bulk metallic glasses, J. Alloy. Compd. 692 (2017) 745–757 https://doi.org/10.1016/j.jallcom.2016.09.033.
[30] A. Concustell, G. Alcalá, S. Mato, T.G. Woodcock, A. Gebert, J. Eckert, M.D. Baró, Effect of relaxation and primary nanocrystallization on the mechanical properties of $Cu_{60}Zr_{22}Ti_{18}$ bulk metallic glass, Intermetallics 13 (2005) 1214–1219 https://doi.org/10.1016/j.intermet.2005.04.003.
[31] C.H. Rycroft, E. Bouchbinder, Fracture toughness of metallic glasses: annealing-induced embrittlement, Phys. Rev. Lett 109 (2012) 194301https://doi.org/10.1103/physrevlett.109.194301.
[32] Z.Q. Chen, L. Huang, F. Wang, P. Huang, T.J. Lu, K.W. Xu, Suppression of annealing-induced embrittlement in bulk metallic glass by surface crystalline coating, Mater. Des 109 (2016) 179–185 https://doi.org/10.1016/j.matdes.2016.07.069.
[33] P. Murali, U. Ramamurty, Embrittlement of a bulk metallic glass due to sub-T_g annealing, Acta Mater 53 (2005) 1467–1478 https://doi.org/10.1016/j.actamat.2004.11.040.
[34] J. Fornell, N.V. Steenberge, A. Varea, E. Rossinyol, E. Pellicer, S. Suriñach, M.D. Baró, J. Sort, Enhanced mechanical properties and in vitro corrosion behavior of amorphous and devitrified $Ti_{40}Zr_{10}Cu_{38}Pd_{12}$ metallic glass, J. Mech. Behav. Biomed. 4 (2011) 1709–1717 https://doi.org/10.1016/j.jmbbm.2011.05.028.
[35] S. González, E. Pellicer, S. Suriñach, M.D. Baró, J. Sort, Mechanical and corrosion behaviour of as-cast and annealed $Zr_{60}Cu_{20}Al_{10}Fe_5Ti_5$ bulk metallic glass, Intermetallics 28 (2012) 149–155 https://doi.org/10.1016/j.intermet.2012.04.007.
[36] H.X. Li, S. Yi, Corrosion behaviors of bulk metallic glasses $Fe_{66.7}C_{7.0}Si_{3.3}B_{5.5}P_{8.7}Cr_{2.3}Al_{2.0}Mo_{4.5}$ having different crystal volume fractions, Mater. Chem. Phys 112 (2008) 305–309 https://doi.org/10.1016/j.matchemphys.2008.05.061.
[37] J.L. Tang, L.S. Yu, J.C. Qiao, Y.Y. Wang, H. Wang, M. Duan, M. Chamas, Effect of atomic mobility on the electrochemical properties of a $Zr_{58}Nb_3Cu_{16}Ni_{13}Al_{10}$ bulk metallic glass, Electrochim. Acta 267 (2018) 222–233 https://doi.org/10.1016/j.electacta.2018.02.071.
[38] Y.X. Zhuang, T.F. Duan, H.Y. Shi, Calorimetric study of non-isothermal crystallization kinetics of $Zr_{60}Cu_{20}Al_{10}Ni_{10}$ bulk metallic glass, J. Alloys Compd 509 (2011) 9019–9025 https://doi.org/10.1016/j.jallcom.2011.06.112.
[39] W.K. An, A.H. Cai, J.H. Li, Y. Luo, T.L. Li, X. Xiong, Y. Liu, Y. Pan, Glass formation and non-isothermal crystallization of $Zr_{62.5}Al_{12.1}Cu_{7.95}Ni_{17.45}$ bulk metallic glass, J. Non-Cryst. Solids 355 (2009) 1703–1706 https://doi.org/10.1016/j.jnoncrysol.2009.06.040.
[40] N.B. Hua, W.Z. Chen, X.L. Liu, F. Yue, Isochronal and isothermal crystallization kinetics of Zr-Al-Fe glassy alloys: effect of high-Zr content, J. Non-Cryst. Solids 388 (2014) 10–16 https://doi.org/10.1016/j.jnoncrysol.2014.01.013.
[41] M.L. Vaillant, V. Keryvin, T. Rouxel, Y. Kawamura, Changes in the mechanical properties of a $Zr_{55}Cu_{30}Al_{10}Ni_5$ bulk metallic glass due to heat treatments below 540°C, Scripta Mater 47 (2002) 19–23 https://doi.org/10.1016/S1359-6462(02)00091-X.
[42] M. Zhou, K. Hagos, H. Huang, L.Ma M.Yang, Improved mechanical properties and pitting corrosion resistance of $Zr_{65}Cu_{17.5}Fe_{10}Al_{7.5}$ bulk metallic glass by isothermal annealing, J. Non-Cryst. Solids 452 (2016) 50–56 https://doi.org/10.1016/j.jnoncrysol.2016.08.014.
[43] M. Song, Y. He, Effect of isothermal annealing on the compressive strength of a ZrAlNiCuNb metallic glass, J. Alloys Compd 509 (2011) 2606–2610 https://doi.org/10.1016/j.jallcom.2010.11.114.
[44] F.X. Qin, X.M. Wang, A. Inoue, Effect of annealing on microstructure and mechanical property of a Ti-Zr-Cu-Pd bulk metallic glass, Intermetallics 15 (2007) 1337–1342 https://doi.org/10.1016/j.intermet.2007.04.005.
[45] Y. Gu, Z. Zheng, S. Niu, W. Ge, Y. Wang, The seawater corrosion resistance and mechanical properties of $Cu_{47.5}Zr_{47.5}Al_5$ bulk metallic glass and its composites, J. Non-Cryst. Solids 380 (2013) 135–140 https://doi.org/10.1016/j.jnoncrysol.2013.08.030.
[46] X. Li, Y. Wang, C. Du, B. Yan, Corrosion behaviors of amorphous and nanocrystalline Fe-based alloys in NaCl solution, J. Nanosci. Nanotechnol. 10 (2010) 7226–7230 https://doi.org/10.1166/jnn.2010.2789.
[47] Y.F. Wu, W.C. Chiang, J.K. Wu, Effect of crystallization on corrosion behavior of $Fe_{40}Ni_{38}B_{18}Mo_4$ amorphous alloy in 3.5% sodium chloride solution, Mater. Lett 62 (2008) 1554–1556 https://doi.org/10.1016/j.matlet.2007.09.047.
[48] B.A. Green, R.V. Steward, I. Kim, C.K. Choi, P.K. Liaw, K.D. Kihm, Y. Yokoyama, In situ observation of pitting corrosion of the $Zr_{50}Cu_{40}Al_{10}$ bulk metallic glass,

Intermetallics 17 (2009) 568–571 https://doi.org/10.1016/j.intermet.2008.12.011.
[49] V. Schroeder, R.O. Ritchie, Stress-corrosion fatigue-crack growth in a zr-based bulk amorphous metal, Acta Mater 54 (2006) 1785–1794 https://doi.org/10.1016/j.actamat.2005.12.006.
[50] A. Kawashima, H. Kurishita, H. Kimura, A. Inoue, Effect of chloride ion concentration on the fatigue crack growth rate of a $Zr_{55}Al_{10}Ni_5Cu_{30}$ bulk metallic lass, Mater. Trans 48 (2007) 1969–1972 https://doi.org/10.2320/matertrans.MRP2007085.
[51] A. Kawashima, Y. Yokoyama, A. Inoue, Zr-based bulk glassy alloy with improved resistance to stress corrosion cracking in sodium chloride solutions, Corros. Sci 52 (2010) 2950–2957 https://doi.org/10.1016/j.corsci.2010.05.007.